Dynamics of Self-Dual Kagome Metamaterials and the Emergence of Fragile Topology

Pegah Azizi,[1] Siddhartha Sarkar,[2] Kai Sun,[2] and Stefano Gonella[1,*]
[1]*Department of Civil, Environmental, and Geo- Engineering, University of Minnesota, Minneapolis, Minnesota 55455, USA*
[2]*Department of Physics, University of Michigan, Ann Arbor, Michigan 48109, USA*

(Received 16 November 2022; revised 30 January 2023; accepted 22 March 2023; published 12 April 2023)

Recent years have seen the discovery of systems featuring fragile topological states. These states of matter lack certain protection attributes typically associated with topology and are therefore characterized by weaker signatures that make them elusive to observe. Moreover, they are typically confined to special symmetry classes and, in general, rarely studied in the context of phononic media. In this Letter, we theoretically predict the emergence of fragile topological bands in the spectrum of a twisted kagome elastic lattice with threefold rotational symmetry, in the so-called self-dual configuration. A necessary requirement is that the lattice is a structural metamaterial, in which the role of the hinges is played by elastic finite-thickness ligaments. The interplay between the edge modes appearing in the band gaps bounding the fragile topological states is also responsible for the emergence of corner modes at selected corners of a finite hexagonal domain, which qualifies the lattice as a second-order topological insulator. We demonstrate our findings through a series of experiments via 3D scanning laser doppler vibrometry conducted on a physical prototype. The selected configuration stands out for its remarkable geometric simplicity and ease of physical implementation in the panorama of dynamical systems exhibiting fragile topology.

DOI: 10.1103/PhysRevLett.130.156101

Topological insulators (TIs), materials with a gapped band structure characterized by topological invariants, have gained increasing attention due to their unique topologically protected edge dynamics. As a result of the so-called bulk-boundary correspondence, they can support edge and interface modes that are immune to backscattering and robust against perturbations and defects. Recent studies have introduced a new class of so-called fragile topological states [1–12]. A set of m frequency bands of a Hamiltonian with some symmetries is called fragile topological if the bands cannot be represented by symmetric (constrained by the symmetries of the Hamiltonian) exponentially localized Wannier functions (SLWF)—generalization of atomic orbitals—in real space; but addition of n trivial bands to those bands allows for representation of the total $(m+n)$ bands by SLWF [1–3,6]. This is in contrast to conventional topological bands where addition of trivial bands does not trivialize the topology. This fragility of the topology means that there cannot exist robust edge states protected by the nontrivial topology at the boundary. However, fragile topological systems in two dimensions are predicted to have corner modes [3,5,8,13].

Another class of systems of interest in topological mechanics is Maxwell lattices, which have an equal number of degrees of freedom and constraints in the bulk [14,15] and are therefore on the verge of mechanical instability [16–19]. A typical example in two dimensions is the kagome lattice, whose unit cell consists of two triangles pinned at a vertex and relatively rotated [20]. Several studies have addressed the mechanical properties [20–26] and wave propagation characteristics [27–30] of these lattices under a variety of cell shapes and effective hinge conditions. Relevant work has studied the faith of mechanical and topological properties in the transition from ideal configurations featuring perfect hinges to structural lattices, as they would be obtained via machining, cutting, or 3D printing. It has been shown that the topological polarization is preserved, albeit diluted, and the zero modes are shifted to finite frequencies [31,32]. Fruchart *et al.* [33] showed that twisted kagome lattices exhibit a special type of duality, whereby a hidden symmetry guarantees that any pair of configurations that are symmetrically located (in configuration space) with respect to a critical configuration referred to as *self-dual*, display identical phonon spectra—a condition that is, however, relaxed working with nonideal lattices of beams [34]. The self-dual case presents peculiar dynamics, with a twofold degenerate spectrum over the entire Brillouin zone (BZ).

In this Letter, we delve deeper into the dynamics of self-dual kagome lattices in search for additional emerging behavior that can be linked to their topology. In the vein of the above-mentioned discourse on structural lattices, we study the case where the cell is modeled as a 2D elastodynamic continuum, which yields a dramatic reconfiguration of the band gap (BG) landscape compared to the ideal case. Our main goal is to determine whether this transition leads to the emergence of new phenomena rooted in topology. Specifically, using topological quantum chemistry (TQC) arguments, we aim at documenting the emergence of fragile topological states at finite frequencies,

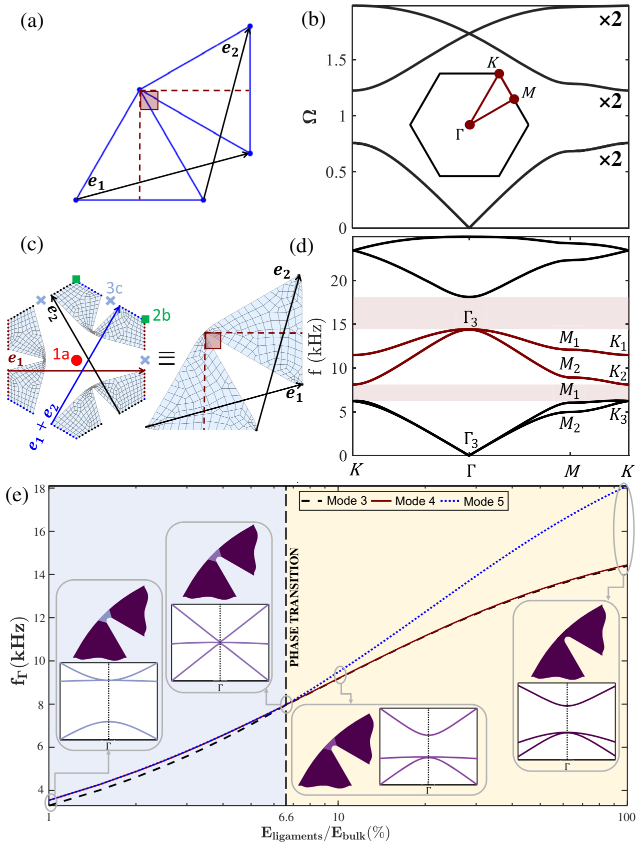

FIG. 1. (a) Geometry of ideal self-dual twisted kagome unit cell. (b) Corresponding band diagram with first BZ shown in inset. (c) Wigner-Seitz unit cell (left) of structural self-dual twisted kagome lattice, labeled with red dot, green square, and blue cross markers representing $1a$, $2b$, and $3c$ Wyckoff positions, respectively, and its equivalent conventional unit cell (right). (d) Corresponding band diagram with emerging isolated modes 3 and 4 highlighted in maroon. The labels denote irrep at HSPs for the first four bands. The corresponding mode shapes are shown in the Supplemental Material, Sec. 1. [37]) (e) Effects of the ligaments softening ($r = E_{\text{ligaments}}/E_{\text{bulk}}$) on the frequency f_Γ of the HSP Γ for bands 3–5, with insets showing the neighborhood of the hinge and the corresponding band diagram near Γ, color coded proportionally to the softness ratio.

an extremely rare occurrence in phononic media, as detailed in [35]. As a by-product of the band reconfiguration, we also report the availability of two spectrally distinct sets of corner modes characterized by different degrees of robustness.

Figure 1(a) shows the unit cell of a twisted kagome lattice comprising two 90°-rotated equilateral triangles, a configuration known as self-dual [33], with $\mathbf{e}_1$ and $\mathbf{e}_2$ denoting the primitive lattice vectors. Here, the lattice consists of rods supporting only tension or compression connected with ideal hinges that allow free rotation. The corresponding band diagram, shown in Fig. 1(b), features a twofold degenerate spectrum over the entire BZ, shown in the inset, with three pairs of overlapping bands and a double Dirac cone at the high symmetry point (HSP) Γ between bands 3–6. The frequency is normalized as $\Omega = \omega/\omega_\circ$, where $\omega_\circ = \pi/L\sqrt{E/\rho}$ is the first natural frequency of a rod of length L, Young's modulus E and density ρ. Figure 1(c) documents the transition to a structural lattice configuration, in which the triangles are elastic domains and the role of the hinges is played by finite-thickness ligaments. These changes induce a profound reconfiguration of the band structure [Fig. 1(d)], whereby (i) the twofold degenerate spectrum is lifted, (ii) a second BG is opened between bands 4 and 5, leading to the appearance of two isolated finite frequency modes, and (iii) a quadratic band crossing is observed at the HSP Γ, between the third and the fourth bands. We also study the evolution of the band diagram upon progressive softening of the hinges in order to reveal the existence of possible phase transitions. We introduce softening by reducing the Young's modulus of the material in the immediate neighborhood of the hinges, as captured by the ratio $r = E_{\text{ligaments}}/E_{\text{bulk}}$ where, for instance, $r = 1\%$ yields very soft hinges while $r = 100\%$ returns the monomaterial cell. Specifically, here we monitor the frequencies f_Γ of bands 3–5 at the HSP Γ, whose evolution with r is illustrated in Fig. 1(e). We find that, as the hinge properties evolve, the gap closes and reopens at a certain value of the control parameter (here $\backsim 6.6\%$), with the quadratic crossing migrating from below to above the gap, which unequivocally denotes a phase transition. The insets show, for a few selected configurations, the immediate neighborhood of the hinge along with the corresponding band diagram (zoom on the neighborhood of the HSP Γ) with hinge and bands color-coded proportionally to r. Interestingly, at the critical point, the band crossing becomes linear and exhibits a threefold degeneracy with an almost flat band (Dirac-like cone). Recently, an analogous linear regime in the neighborhood of Dirac points has been demonstrated for periodic origami using a dynamic homogenization framework [36].

We now claim that the nature of the above-mentioned phase transition is topological. Specifically, reopening the BG induces fragile topological states within bands 3 and 4 protected by threefold rotation symmetry C_3. This can be shown using the recently developed method of symmetry indicators [40,41], band structure combinatorics [42], and TQC [43,44]. This method provides a full classification of topological states protected by spatial symmetries, and can detect any such topological states by investigating how the eigenfunctions of the bands transform under symmetries, i.e., the representation labels of the eigenfunctions, at the HSPs of the BZ. Conveniently, all possible representation labels that a set of bands generated by SLWF can feature are tabulated in the Bilbao crystallography server (BCS) [45–49]. We note that our system falls under $G = p31m$ wallpaper group. The HSPs Γ, K, and M [inset of Fig. 1(b)] have little co-groups C_{3v}, C_{3v}, and C_s, respectively. The eigenfunctions at these HSPs transform under the representations of the corresponding little co-group. From FEM, we find that degenerate eigenfunctions at the Γ point of bands 3–4 transform under 2D irreducible representation (irrep) Γ_3, the eigenfunctions at M transform under 1D irreps M_2 and M_1, and the eigenfunctions at K transform under 1D irreps K_2 and K_1, as denoted in Fig. 1(d) (see also Supplemental Material, Sec. 1 [37] for corresponding eigenfunctions). BCS tables reveal that these irreps cannot be represented by any SLWF, which implies that these two bands are topological [43]; as a result, the change in behavior observed at $r = 6.6\%$ in Fig. 1(e) can be qualified as a topological phase transition. Specifically, the irreps of bands 3–4 are consistent with the formal *difference*:

$$({}^1E^2E\uparrow G)_{2b}\ominus(E\uparrow G)_{1a}, \tag{1}$$

where ${}^1E^2E$ (and E) represents two SLWFs with angular momentum 1 (p_x and p_y type orbitals), where $1a$ and $2b$ are Wyckoff positions shown in Fig. 1(c). In words, this means that irrep labels for bands 3 and 4 are consistent with the *difference* between $p_x - p_y$ type orbitals at position $2b$ [see Fig. 1(c); position $2b$ has multiplicity 2 in the unit cell, so in total 4 orbitals in the unit cell] and $p_x - p_y$ type orbitals at position $1a$ (position $1a$ has multiplicity 1 in the unit cell, in total 2 orbitals in the unit cell). Furthermore, since the irrep labels of the bands 1–2 are $\Gamma_3 - M_1 \oplus M_2 - K_3$ and are consistent with the SLWFs $(E\uparrow G)_{1a}$ (which renders bands 1–2 topologically trivial), together bands 1–4 can be represented by SLWFs $({}^1E^2E\uparrow G)_{2b}$, meaning that bands 1–4 together are topologically trivial. This is the distinguishing characteristic of fragile topological bands—the addition of trivial bands to them render the topology trivial [6]. We also verify the topological nontriviality of bands 3–4 by calculating the winding of hexagonal Wilson loop (WL) [2] (see Supplemental Material, Sec. 2 [37] for details of WL calculation). Importantly, here the fragile topology of bands 3–4 is protected by C_3 (that this fragile topology only depends on C_3, not the mirrors can be understood from the fact that, if we break the mirror symmetry perturbatively such that bands 3–4 are still isolated from other bands, the irrep labels at the HSPs would be $\Gamma_2 \oplus \Gamma_3 - 2M_1 - 2K_1$, which also correspond to fragile topological bands [6]). It is worth noting that the fragile topology of bands 3–4 can be detected just from the band connectivity, namely, from the fact that there is a degeneracy at Γ and no degeneracy at K—something that trivial bands (that can be represented by SLWF) cannot display, as detailed in Supplemental Material, Sec. 3 [37]. This makes the detection of C_3 symmetry protected fragile bands in wallpaper group $p31m$ considerably easier than any other type of fragile bands where further explicit calculations are required to confirm nontrivial topology.

We now shift our attention to the two BGs bounding bands 3–4, looking for any edge and corner modes comprised therein. We first perform a super-cell analysis on a 15-cell super-cell modeled with the same finite element discretization used for the unit cell analysis. The resulting band diagram is plotted in Fig. 2(a). We observe a pair of degenerate bands in each BG (shaded regions) indicated by green lines. The supercell mode shapes at $\xi = 0$ and $\xi = \pi$ within the first and the second BGs (marked by the green markers) are displayed in Figs. 2(b)–2(e), respectively. The high decay rate and the occurrence of localization at two opposite edges qualify these branches as nonpolarized edge modes, as expected for a twisted kagome lattice (see Supplemental Material, Sec. 4 [37] for details). We then calculate eigenfrequencies and mode shapes for a finite hexagon-shaped domain as shown in Figs. 2(g) and 2(i). The eigenfrequencies in intervals encompassing the two BGs are shown in Figs. 2(f) and 2(h). The insets zoom in on two sets of three degenerate modes inside the second ($f = 16.01$ kHz) and first ($f = 7.34$ kHz) BG; the corresponding mode shapes depicted in Figs. 2(g) and 2(i), obtained by superposition of the degenerate modes, reveal localization of deformation at the corners of the hexagon, which qualifies these as corner modes and the lattice as 2D second-order TI. Interestingly, the two sets of mode shapes feature localization at alternating corners and have distinct morphological characteristics. Specifically, corner modes appearing in the first BG have lower decay rate, likely due to their higher proximity to (and contamination from) the bulk band and the edge modes observable in the top region of the gap. Conversely, the second BG corner modes show stronger localization. Additional evidence of these differences is found via full-scale transient simulations, in which we excite the bottom-right corner (marked by a black star) with 30-cycle narrow-band tone burst force excitations with carrier frequencies at 16.01 and 7.34 kHz, corresponding to the second BG and first BG corner modes, respectively [time histories and spectra are depicted in Figs. 2(m), 2(q), 2(l), and 2(p)]. For each carrier, two snapshots of the resulting wave fields are shown in Figs. 2(j) and 2(k) for the second BG and Figs. 2(n) and 2(o) for the first BG. For the second BG, we observe localization in the neighborhood of the excitation point, matching the mode shape pattern in Fig. 2(g) and confirming the notion that the second BG corner modes minimally leak into edge and bulk modes. In contrast, the wave field for the first BG corner modes shows opposite dynamics: while in the early time snapshot of Fig. 2(n) some degree of localization is established around the excitation point, the signal travels along the edge and eventually migrates to the adjacent corner, as seen in Fig. 2(o). This transfer can be explained by the combination of three factors: the lack of a corner mode for the excited corner in the first BG, the availability of a corner mode, at that same frequency, in the adjacent corner, and the spectral

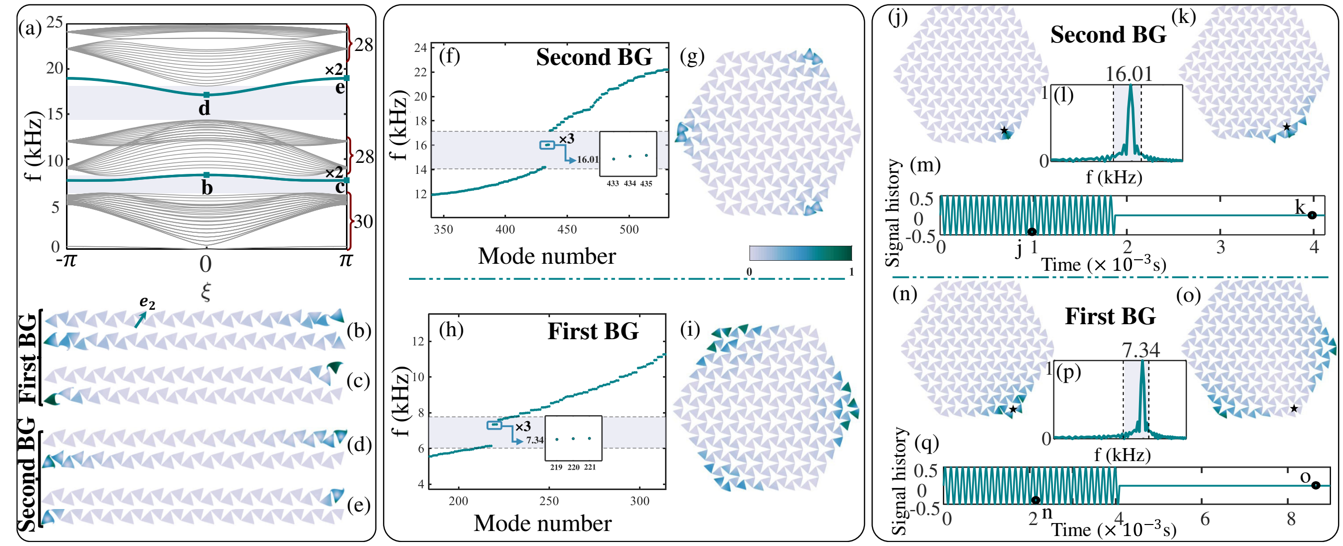

FIG. 2. (a) Band diagram of a 15-cell structural self-dual twisted kagome supercell with Bloch-periodic boundary condition along $\mathbf{e}_2$ and open boundary condition along $\mathbf{e}_1$. (b)–(e) Mode shapes of degenerate edge mode pairs, sampled at $\xi = 0, \pi$ and highlighted with green markers, within the first (b)–(c) and second (d)–(e) BG. (f)–(g) Eigenfrequencies (f) in an interval encompassing the second BG, with three degenerate modes at $f = 16.01$ kHz, highlighted in the inset, and corresponding corner mode (from linear superposition of the degenerate modes) shown in (g). (j)–(m) Snapshots of wave fields for narrow-band burst excitation with carrier frequency at $\sim$16.01 kHz in the second BG [signal in (m) and corresponding spectrum in (l)], during the 30-cycle energy pumping stage (j) and relaxation time (k) of the excitation. The wave fields suggest strong localization of the second BG corner modes. (h)–(i),(n)–(q) Same quantities discussed in (f)–(g),(j)–(m) for corner modes in the first BG at 7.34 kHz. The wave fields suggest weak corner localization promoted by activation of edge modes. Colors are proportional to the in-plane displacement normalized by the maximum value.

proximity of the signal carrier to prominent edge modes. We note that, while no formal connection can be claimed between fragile topological states and edge or corner modes in the absence of a proper bulk-edge correspondence for fragile topology, the availability of localized modes is in itself a by-product (of this band structure) of practical relevance, e.g., for vibration isolation and harvesting applications.

We substantiate our theoretical findings—emergence of fragile topological states and establishment of corner modes—through laser vibrometry experiments on a physical prototype, see setup in Fig. 3(a). All details on fabrication, vibrometer specifications, and setup are provided in Supplemental Material, Secs. 5–7 [37]. First, we want to demonstrate experimentally the opening of the second BG, which is absent in the ideal self-dual kagome lattice, as a result of the finite-thickness hinges of the structural metamaterial. To this end, we prescribe a broadband pseudorandom excitation at the point marked by the yellow dot [Fig. 3(a)], measure the in-plane velocity at the designated sampling points inside the green box [Fig. 3(a)], and normalize the average value by that of the excitation point to construct a curve of transmissibility versus frequency, plotted in Fig. 3(b). An analogous curve, plotted in Fig. 3(c), is obtained via full-scale steady-state simulation under sustained harmonic excitation. Both curves, in reasonable agreement, feature two distinct regions of attenuation, highlighted in light purple, supporting the existence of finite-frequency isolated band(s) in the midfrequency spectrum. The attenuation intervals are in satisfactory agreement with the BGs predicted via Bloch analysis [Fig. 1(d)]. See also Supplemental Material, Sec. 8 [37] for details on the discrepancies between experiments and theory.

We now seek evidence of the fragile topological nature of the intermediate bands by experimentally reconstructing the morphological characteristics of the bands. To this end, we collect the time histories of the lateral in-plane velocity at evenly distanced points along the Γ-*K* direction [red dots in the insets of the Figs. 3(d) and 3(e), for experiment and simulation, respectively] for several tone burst excitation signals with different carrier frequencies within the passband regions. Subsequently, we perform 2D discrete Fourier transform (2D-DFT) on each spatiotemporal dataset and we aggregate all the resulting spectral amplitude contours and superimpose them on the band diagram (see Supplemental Material, Sec. 9 [37] for full depiction). Overall the contours of the bursts populate the spectral plane in a way that follows the morphological attributes of the band diagram. Focusing on the midfrequency range, the peculiar shape of the third and fourth modes associated with fragile topology, featuring the bands crossing at Γ without retouching elsewhere at the boundary of the BZ (or at the other HSPs) is captured perfectly. Finally, we conduct three experiments with three distinct tone bursts (applied at the bottom corner) at three carrier frequencies falling in the

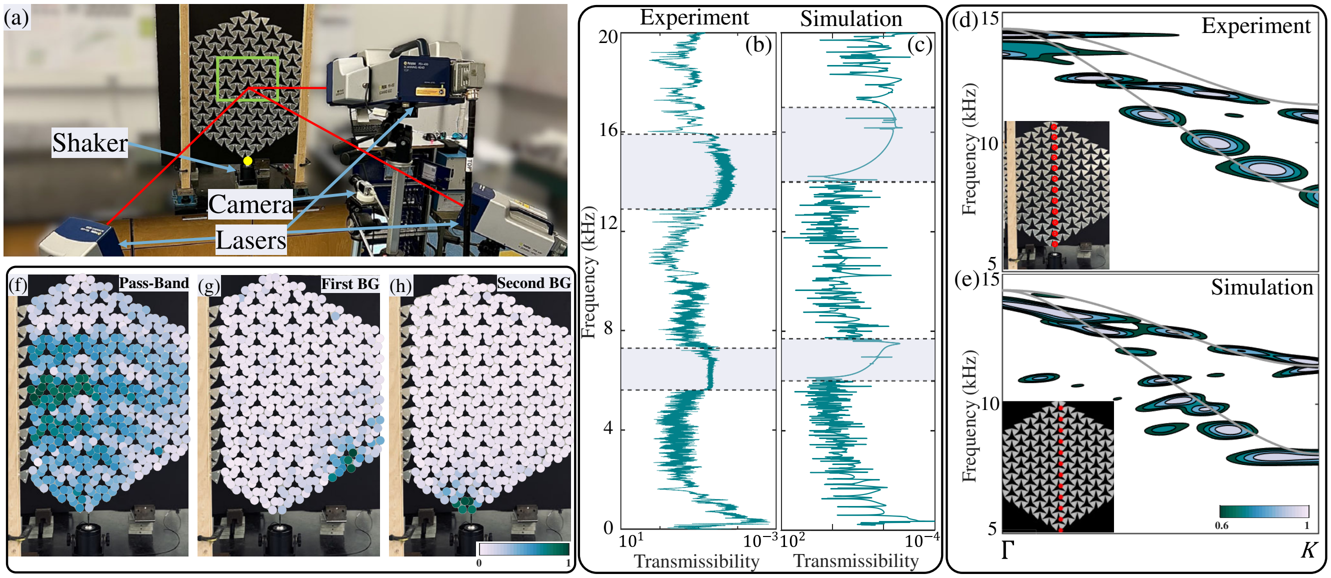

FIG. 3. (a) Experimental setup for 3D SLDV testing of structural self-dual twisted kagome hexagonal prototype. (b)–(c) Experimental (b) and simulation (c) transmissibility curve with regions of attenuation highlighted in light purple. (d)–(e) Optical mode reconstruction from experimental (d) and simulation (e) data; the reconstruction involves collecting time histories at the sampling points marked by red dots in the insets and subjecting them to 2D-DFT, repeating the procedure for several carrier frequencies in the interval of interest. The 2D-DFT yields spectral amplitude contours, here superimposed to the band diagram to highlight modal activation. (f)–(h) Snapshots of the wave fields induced through burst excitations within the passband (f), and at the frequencies of the first (g) and second (h) BGs corner modes, respectively, with color bar referring to the velocity amplitude. 2D DFT and wave field data are normalized by the highest value and proportionally color coded.

acoustic passband, first BG and second BG. The objective here is to reconstruct experimentally the wave propagation patterns established in different frequency regimes and document the establishment of corner modes. In Fig. 3(f) a carrier frequency of ~3 kHz generates a wave field that propagates through the bulk, which is the signature of passband behavior. For an excitation in the first BG [Fig. 3(g)], we observe wave propagation along the edge and accumulation at the next available corner. The behavior is consistent with the localized modal landscape in the first BG, in which the corner modes do not appear at the set of corners that include the excitation point and, moreover, well-defined edge modes exist in the gap. In contrast, for excitation in the second BG, we observe a highly localized and persistent corner mode [Fig. 3(h)], even after long relaxation times for the bursts.

P. A. acknowledges support of the UMN CSE Graduate Fellowship. S. G. acknowledges support from the National Science Foundation (Grant No. CMMI-2027000). S. S. and K. S. acknowledge support from the Office of Naval Research (Grant No. MURI N00014-20-1-2479).

---

[*] sgonella@umn.edu

[1] H. C. Po, H. Watanabe, and A. Vishwanath, Phys. Rev. Lett. **121**, 126402 (2018).
[2] B. Bradlyn, Z. Wang, J. Cano, and B. A. Bernevig, Phys. Rev. B **99**, 045140 (2019).
[3] J. Ahn, S. Park, and B.-J. Yang, Phys. Rev. X **9**, 021013 (2019).
[4] A. Bouhon, A. M. Black-Schaffer, and R.-J. Slager, Phys. Rev. B **100**, 195135 (2019).
[5] B. J. Wieder and B. A. Bernevig, arXiv:1810.02373.
[6] Z.-D. Song, L. Elcoro, and B. A. Bernevig, Science **367**, 794 (2020).
[7] V. Peri, Z.-D. Song, M. Serra-Garcia, P. Engeler, R. Queiroz, X. Huang, W. Deng, Z. Liu, B. A. Bernevig, and S. D. Huber, Science **367**, 797 (2020).
[8] B. J. Wieder, Z. Wang, J. Cano, X. Dai, L. M. Schoop, B. Bradlyn, and B. A. Bernevig, Nat. Commun. **11**, 627 (2020).
[9] B. Lian, F. Xie, and B. A. Bernevig, Phys. Rev. B **102**, 041402(R) (2020).
[10] A. Bouhon, T. Bzdušek, and R.-J. Slager, Phys. Rev. B **102**, 115135 (2020).
[11] M. B. de Paz, M. G. Vergniory, D. Bercioux, A. García-Etxarri, and B. Bradlyn, Phys. Rev. Res. **1**, 032005(R) (2019).
[12] V. Peri, Z.-D. Song, B. A. Bernevig, and S. D. Huber, Phys. Rev. Lett. **126**, 027002 (2021).
[13] J. L. Manes, Phys. Rev. B **102**, 024307 (2020).
[14] J. C. Maxwell, J. C. Maxwell, Philos. Mag. **27**, 294 (1864).
[15] C. Calladine, Int. J. Solids Struct. **14**, 161 (1978).
[16] A. Souslov, A. J. Liu, and T. C. Lubensky, Phys. Rev. Lett. **103**, 205503 (2009).
[17] X. Mao and T. C. Lubensky, Annu. Rev. Condens. Matter Phys. **9**, 413 (2018).

[18] X. Mao and T. C. Lubensky, Phys. Rev. E **83**, 011111 (2011).

[19] T. C. Lubensky, C. L. Kane, X. Mao, A. Souslov, and K. Sun, Rep. Prog. Phys. **78**, 073901 (2015).

[20] K. Sun, A. Souslov, X. Mao, and T. C. Lubensky, Proc. Natl. Acad. Sci. U.S.A. **109**, 12369 (2012).

[21] N. A. Fleck and X. Qiu, J. Mech. Phys. Solids **55**, 562 (2007).

[22] S. Hyun and S. Torquato, J. Mater. Res. **17**, 137 (2002).

[23] S. Arabnejad and D. Pasini, Int. J. Mech. Sci. **77**, 249 (2013).

[24] Y. Zhang, X. Qiu, and D. Fang, Int. J. Solids Struct. **45**, 3751 (2008), special Issue Honoring K. C. Hwang.

[25] D. D. Symons and N. A. Fleck, J. Appl. Mech. **75**, 051011 (2008).

[26] H. Danawe, H. Li, K. Sun, and S. Tol, Phys. Rev. Lett. **129**, 204302 (2022).

[27] H. Chen, H. Nassar, A. N. Norris, G. K. Hu, and G. L. Huang, Phys. Rev. B **98**, 094302 (2018).

[28] E. Riva, D. E. Quadrelli, G. Cazzulani, and F. Braghin, J. Appl. Phys. **124**, 164903 (2018).

[29] M. Schaeffer and M. Ruzzene, J. Appl. Phys. **117**, 194903 (2015).

[30] A. S. Phani, J. Woodhouse, and N. A. Fleck, J. Acoust. Soc. Am. **119**, 1995 (2006).

[31] M. Charara, K. Sun, X. Mao, and S. Gonella, Phys. Rev. Appl. **16**, 064011 (2021).

[32] J. Ma, D. Zhou, K. Sun, X. Mao, and S. Gonella, Phys. Rev. Lett. **121**, 094301 (2018).

[33] M. Fruchart, Y. Zhou, and V. Vitelli, Nature (London) **577**, 636 (2020).

[34] S. Gonella, Phys. Rev. B **102**, 140301(R) (2020).

[35] Y. Xu, M. G. Vergniory, D.-S. Ma, J. L. Mañes, Z.-D. Song, B. A. Bernevig, N. Regnault, and L. Elcoro, arXiv: 2211.11776.

[36] O. Oudghiri-Idrissi and B. B. Guzina, Comput. Methods Appl. Mech. Eng. **399**, 115386 (2022).

[37] See Supplemental Material at http://link.aps.org/supplemental/10.1103/PhysRevLett.130.156101 for details, including the following: Mode shapes of the lowest bands and their irreps, Wilson loop calculation, irreps of the wallpaper group $p31m$ and band connectivity, edge modes explanation, material properties and details on the experimental procedure, and a note on the 2D DFT, which includes Refs. [38,39].

[38] M. S. Dresselhaus, G. Dresselhaus, and A. Jorio, *Group Theory: Application to the Physics of Condensed Matter* (Springer-Verlag Berlin Heidelberg, 2007).

[39] A. Alexandradinata, X. Dai, and B. A. Bernevig, Phys. Rev. B **89**, 155114 (2014).

[40] H. C. Po, A. Vishwanath, and H. Watanabe, Nat. Commun. **8**, 50 (2017).

[41] E. Khalaf, H. C. Po, A. Vishwanath, and H. Watanabe, Phys. Rev. X **8**, 031070 (2018).

[42] J. Kruthoff, J. de Boer, J. Van Wezel, C. L. Kane, and R.-J. Slager, Phys. Rev. X **7**, 041069 (2017).

[43] B. Bradlyn, L. Elcoro, J. Cano, M. G. Vergniory, Z. Wang, C. Felser, M. I. Aroyo, and B. A. Bernevig, Nature (London) **547**, 298 (2017).

[44] J. Cano, B. Bradlyn, Z. Wang, L. Elcoro, M. G. Vergniory, C. Felser, M. I. Aroyo, and B. A. Bernevig, Phys. Rev. B **97**, 035139 (2018).

[45] M. I. Aroyo, J. M. Perez-Mato, D. Orobengoa, E. Tasci, G. de la Flor, and A. Kirov, Bulg. Chem. Commun. **43**, 183 (2011).

[46] M. I. Aroyo, J. M. Perez-Mato, C. Capillas, E. Kroumova, S. Ivantchev, G. Madariaga, A. Kirov, and H. Wondratschek, Z. Kristallogr.-Cryst. Mater. **221**, 15 (2006).

[47] M. I. Aroyo, A. Kirov, C. Capillas, J. Perez-Mato, and H. Wondratschek, Acta Crystallogr. Sect. A **62**, 115 (2006).

[48] M. G. Vergniory, L. Elcoro, Z. Wang, J. Cano, C. Felser, M. I. Aroyo, B. A. Bernevig, and B. Bradlyn, Phys. Rev. E **96**, 023310 (2017).

[49] L. Elcoro, B. Bradlyn, Z. Wang, M. G. Vergniory, J. Cano, C. Felser, B. A. Bernevig, D. Orobengoa, G. Flor, and M. I. Aroyo, J. Appl. Crystallogr. **50**, 1457 (2017).